Applied Catalysis B: Environmental 292 (2021) 120144

Contents lists available at ScienceDirect

Applied Catalysis B: Environmental

journal homepage: www.elsevier.com/locate/apcatb

Metal-free boron and sulphur co-doped carbon nanofibers with optimized p-band centers for highly efficient nitrogen electroreduction to ammonia

Yankun Wen [a], Han Zhu [a,*], Jiace Hao [a], Shuanglong Lu [a], Wei Zong [b], Feili Lai [c], Piming Ma [a], Weifu Dong [a], Tianxi Liu [a,b], Mingliang Du [a,*]

[a] Key Laboratory of Synthetic and Biological Colloids, Ministry of Education, School of Chemical and Material Engineering, Jiangnan University, Wuxi, 214122, PR China

[b] State Key Laboratory for Modification of Chemical Fibers and Polymer Materials, College of Materials Science and Engineering, Innovation Center for Textile Science and Technology, Donghua University, Shanghai, 201620, PR China

[c] Department of Chemistry, KU Leuven, Celestijnenlaan 200F, Leuven, 3001, Belgium

ARTICLE INFO

Keywords:
Metal-free electrocatalysts
S and B co-doped carbon nanofibers
Electrochemical nitrogen reduction
p-Band center
Materials science

ABSTRACT

Herein, we proposed a conceptual and experimental breakthrough in overcoming the high energy barriers for N_2 absorption and activation by tuning the center positions of p_z orbital of boron in S and B co-doped carbon nanofibers (S-B/CNFs). We theoretically and experimentally investigated the influences of nonmetallic elements of B as electron acceptor, and S and P as electron donor on tuning NRR activity. We revealed that the heteroatom-doping of S atoms induced changing of center position of the p_z orbital of B facilitates the adsorption of N_2 on S-C-B sites and reduces the energy barriers for rate-determining steps. The $S_{6.23}$-$B_{8.09}$/CNFs exhibits the highest NRR activity with high Faradaic efficiency of 22.4 % and NH_3 yield of 0.223 μmol h^{-1} cm^{-2} at −0.7 V versus reversible hydrogen electrode. The combined computational and experimental works uncover the relationship between the *p*-band center of heteroatom doped carbon catalysts and NRR activity.

1. Introduction

As important fertilizers, ammonia is one of the most fundamental chemicals for sustaining human life [1]. The conversion of earth-abundant N_2 into NH_3 remains a challenge due to its chemical inertness nature with high bond energy and permanent dipole in the N≡N triple bond [2]. The industrial-scale ammonia synthesis is dominantly operated by the Haber–Bosch process, which should rely on an iron-based catalyst and harsh conditions (high temperature and pressure) [3]. In addition, such process requires tremendous energy consumption and generates massive amounts of greenhouse gases [4–6]. Developing sustainable technology to produce NH_3 under milder conditions remains an elusive scientific and technological aim [7–9].

Currently, the electrochemical nitrogen reduction reaction (NRR) has attracted growing interests as a potential green alternative technology for ammonia production at ambient temperature and pressure [10]. The enormous difference in energy between the highest occupied and lowest unoccupied molecular orbitals of N≡N triple bond strongly hinders electron transfer reactions, leading to sluggish reaction kinetics [11]. Thus, the NRR process requires the advanced electrocatalysts to catalyze the complex six-electron reduction of nitrogen and simultaneously impede the competitive hydrogen evolution reaction (HER) [12]. Up to now, the development of NRR electrocatalysts has mainly centered on noble metal, transition metal and their compounds [13–15]. However, the dinitrogen activation is still limited by transition metals owing to the weak nitrogen adsorption [16]. Meanwhile, the *d* orbital in transition metals also involves in the competing HER, resulting in a compromising Faradaic efficiency of NRR [17]. Therefore, developing and constructing high-performance NRR electrocatalysts are highly desirable due to the unsatisfactory conversion efficiency and poor production rate [18].

The design of metal-free catalysts, such as carbon-based materials, is a promising strategy to promote the NRR efficiency due to their low cost, excellent stability, mechanical flexibility and good electrical conductivity [19]. Moreover, endowing carbon-based catalysts with sufficient catalytic centers still remains a grand challenge [20]. Introducing heteroatoms into carbon matrix has drawn significant attention due to the increased positive charge density on adjacent carbon atoms by structural distortion [21]. For example, the Boron in B-doped carbon with strong electronic affinity can be served as Lewis acid sites to capture the lone

* Corresponding authors.
E-mail addresses: zhysw@jiangnan.edu.cn (H. Zhu), du@jiangnan.edu.cn (M. Du).

https://doi.org/10.1016/j.apcatb.2021.120144
Received 25 January 2021; Received in revised form 8 March 2021; Accepted 14 March 2021
Available online 17 March 2021

pair electrons of nitrogen and activate the inert dinitrogen [22]. In addition, the calculated electronic structure analysis indicates that the *p*-orbital of boron matches well with the π*-orbital of N_2 and the p_z orbital of B sites with half full is beneficial to the activation of N_2 [23]. However, the relationship between NRR activity and the center position of p_z orbital of boron lacks of exploration and few reported literature has centered on the regulation of the center position of p_z orbital of B [24].

Herein, we proposed a conceptual and experimental breakthrough in overcoming the high energy barriers for N_2 absorption and activation by tuning the p_z orbital center positions of boron in S and B co-doped carbon nanofibers (S-B/CNFs). The CNFs were served as host and reactor for the controlled adjusting of B, S and P contents, and we theoretically and experimentally investigated the influences of nonmetallic elements of B as electron acceptor, and S and P as electron donor on tuning NRR activity. We revealed that the heteroatom-doping of S atoms induced changing of center position of the p_z orbital of B facilitates the adsorption of N_2 on S-C-B sites and reduces the energy barriers for rate-determining steps of the first protonation to form *NNH. The $S_{6.23}$-$B_{8.09}$/CNFs (S and B contents of 6.23 and 8.09 at%) exhibits the highest NRR activity with high Faradaic efficiency of 22.4 % and NH_3 yield of 0.223 μmol h^{-1} cm^{-2} at −0.7 V versus reversible hydrogen electrode. The combined computational and experimental work uncovers the relationship between the *p*-band center of heteroatom doped carbon catalysts and NRR activity and paves a way for their future application.

2. Experimental section

2.1. Materials

Polyacrylonitrile (PAN, $M_w = 1.49 \times 10^5$) was acquired from Sinopec Shanghai Petrochemical Co., Ltd. *N, N'*-dimethylformamide (DMF), boric acid (H_3BO_3), sodium hypophosphite monohydrate ($Na_3PO_2 \cdot H_2O$), sulfur powder (S), potassium sulfate (K_2SO_4), salicylic acid ($C_7H_6O_3$), sodium citrate dihydrate ($C_6H_5Na_3O_7 \cdot 2H_2O$), sodium nitroferricyanide dehydrate ($C_5FeN_6Na_2O \cdot 2H_2O$), sodium hypochlorite solution (NaClO), and hydrazine monohydrate ($N_2H_4 \cdot H_2O$) were purchased from Sinopharm Chemical Reagent Co., Ltd. Nafion 212 membrane was obtained from Dupont. Nitrogen (N_2, 99.999 %) and argon (Ar, 99.999 %) were bought from Xinxiyi Technology Co., Ltd. (Jiangsu, China). Deionized water (resistivity: ca.18.2 MΩ cm) was used to prepare the electrolyte solutions. All chemicals were analytical grades.

2.2. Synthesis of B/CNFs

PAN and boric acid were added in 15 mL DMF to form uniform solution after continuous stirring at room temperature for 15 h. Then, the solution was transferred to 10 mL plastic syringe with needle (a diameter of 0.7 mm) and the electrospinning was conducted at 16 kV with an injecting rate of 0.4 mL h^{-1} at 40 °C. The collector was a rolling Al foil roller with a distance of 17 cm to the metal needle. The PAN nanofiber mat with boric acid was obtained after 15 h. The as-spun membrane was heated to 230 °C for 3 h in air atmosphere at a heating rate of 5 °C min^{-1}. Next, the furnace was heated to different temperatures (800 °C, 900 °C, and 1000 °C) under argon protection for 3 h at a heating rate of 5 °C min^{-1}.

2.3. Synthesis of S-B/CNFs

PAN and boric acid were added in 15 mL DMF to form uniform solution after continuous stirring at room temperature for 15 h. Then, the solution was transferred to 10 mL plastic syringe with needle (a diameter of 0.7 mm) and the electrospinning was conducted at 16 kV with an injecting rate of 0.4 mL h^{-1} at 40 °C. The collector was a rolling Al foil roller with a distance of 17 cm to the metal needle. The PAN nanofiber mat with boric acid was obtained after 15 h. The as-spun membrane was heated to 230 °C for 3 h in air atmosphere at a heating rate of 5 °C min^{-1}. And the furnace was heated to 400 °C while another boat located at the front end of the Ar flow with S powder was heated to 250 °C and maintained for 2 h. Finally, the furnace was heated to 900 °C under Ar protection for 3 h at a heating rate of 5 °C min^{-1}.

2.4. Synthesis of P-B/CNFs

PAN and boric acid were added in 15 mL DMF to form uniform solution after continuous stirring at room temperature for 15 h. Then, the solution was transferred to 10 mL plastic syringe with needle (a diameter of 0.7 mm) and the electrospinning was conducted at 16 kV with an injecting rate of 0.4 mL h^{-1} at 40 °C. The collector was a rolling Al foil roller with a distance of 17 cm to the metal needle. The PAN nanofiber mat with boric acid was obtained after 15 h. The as-spun membrane was heated to 230 °C for 3 h in air atmosphere at a heating rate of 5 °C min^{-1}. And the furnace was heated to 400 °C while another boat located at the front end of the Ar flow with $Na_3PO_2 \cdot H_2O$ powder was heated to 420 °C and maintained for 2 h. Next, the furnace was heated to 900 °C under Ar protection for 3 h at a heating rate of 5 °C min^{-1}.

2.5. Material characterization

The morphologies of samples were measured with field-emission scanning electron microscopy (FE-SEM, Hitachi S-4800), transmission electron microscopy (TEM, JEM-2100 plus), and high-resolution TEM (HRTEM, FEI titan themis 200 TEM, Bruker super-X EDS, 977 Enfinium-ER EELS). The phase and element composition of samples were characterized by X-ray diffraction (XRD, Bruker AXS D8) with Cu Kα radiation and X-ray photoelectron spectroscopy (XPS, Kratos Axis Ultra DLD) using Al Kα radiation. The contact angle was tested by video optical contact angle measuring instrument (OCA15EC, Dataphysics). The Raman spectra were collected on a Renishaw Raman spectrometer using 532 nm laser. ^1H NMR spectra were recorded on a Bruker 400 with Probe TXI using a 5 mm tube. Temperature-programmed desorption curves (N_2-TPD) were obtained by a MicrotracBEL BELCAT-IIautomatic chemical adsorption instrument. These three samples were first pretreated at 400 °C for 50 min with a 30 sccm Ar stream and then it cooled down to 50 °C under Ar atmosphere. Then, these samples were adsorbed by N_2 for 30 min, and the remaining N_2 was purged by Ar for 30 min. Finally, the N_2 desorption was carried out by heating from 50 °C to 700 °C at a rate of 10 °C min^{-1}.

2.6. Electrochemical measurements

All the electrochemical measurements were performed on a CHI660E electrochemical station in an H-type electrochemical cell. All tests were conducted by using a three electrode system at the room temperature. The Ag/AgCl saturated KCl solution and the Pt wire were used as the reference electrode and the counter electrode. The membrane after calcination in the tube vacuum furnace was cut into square thin pieces, which were fixed on the Teflon motor clip as the working electrode. The two electrolytic cells were connected by 211 Nafion membrane. The purities of all gases (N_2, Ar) used in the experiments were 99.999 %. The potentials in all tests were calibrated by the following equation, E (V *vs.* RHE) = E (V *vs.* Ag/AgCl) + 0.197 + 0.059 × pH. In the nitrogen reduction reaction chronoamperometry experiment, 25 mL of the electrolyte solution was first saturated with N_2 for at least 40 min, and then tested in N_2 saturated 0.5 M K_2SO_4 electrolyte. In every cycling test, the operating condition and environmental condition remain unchanged.

2.7. Determination of ammonia

The concentration of ammonia gas produced by all samples in the experiment was determined by the indophenol blue method [25]. First, 2 mL of the electrolyte solution after two hours of electrolysis in the cathode chamber was taken out, and then added 400 μL of 1 M NaOH

solution with sodium citrate (5 wt%) and salicylic acid (5 wt%). Next, 200 μL of sodium hypochlorite solution (0.05 M) and 200 μL of sodium nitroprusside solution (1 wt%) were added to the above-mentioned mixed solution, and place in a dark place to stand for two hours. The absorption spectrum of the solution was obtained by an UV–vis spectrophotometer under the wavelength range of 500−800 nm. To estimate the NH_4^+ concentration, the calibration curves were constructed using concentrations of 6.25, 12.5, 25, 50, 100 and 200 μmol L^{-1} NH_4Cl solutions.

2.8. Determination of hydrazine

The concentrations of N_2H_4 produced by all samples in the experiment were assessed by the Watt and Chrisp methods [26]. First, 5.99 g of p-(dimethylamino) benzaldehyde, 30 mL of concentrated HCl and 300 mL of ethanol were mixed together as a color reagent. Next, 2 mL of the electrolyte solution and 2 mL of color reagent were mixed and stirred for 15 min under room temperature. The absorption spectrum of the solution was obtained by an UV–vis spectrophotometer under the wavelength range of 400−600 nm. To quantify the N_2H_4 concentration, a calibration curve was obtained using concentrations of 0, 0.125, 0.25, 0.5, 0.1 μg mL^{-1} N_2H_4 solutions.

2.9. Calculation of NH_3 yield and Faradaic efficiency

The Faradaic efficiency was estimated from the charge consumed for NH_3 production and the total charge passed through the electrode:

$$\text{Faradaic efficiency} = 3\ F \times c(NH_4^+) \times V/(17 \times Q)$$

Where F is the Faraday constant (96,485 C mol^{-1}), $c(NH_4^+)$ is the measured concentration of NH_4^+, V is the electrolyte volume, Q is the quantity of applied electricity.

The yield of NH_3 can be calculated as follows:

$$NH_3\ \text{yeild} = c(NH_4^+) \times V/(t \times S)$$

Where $c(NH_4^+)$ is the measured concentration of NH_4^+, V is the electrolyte volume, t is the reaction time, and S is the electrode geometric area.

2.10. DFT calculations

The present first principle DFT calculations were performed by Vienna Ab initio Simulation Package (VASP) with the projector augmented wave (PAW) method [27,28]. The exchange-functional was treated using the generalized gradient approximation (GGA) of Perdew-Burke-Ernzerhof (PBE) functional [29]. DFT-D3 correction method was applied to calculate the van der Waals (vdW) interactions. The energy cutoff for the plane wave basis expansion was set to 450 eV and the force on each atom less than 0.02 eV/Å was set for convergence criterion of geometry relaxation. 6 × 6 supercell of graphene was constructed. A 15 Å vacuum along z direction was employed for each model in order to avoid the interaction between periodic structures. The Brillouin zone integration was performed using 2 × 2×1 k-point sampling through all the computational process. The self-consistent calculations applied a convergence energy threshold of 10^{-4} eV.

The free energies of the N_2 reduction steps were calculated by the equation: $\Delta G = \Delta E_{DFT} + \Delta E_{ZPE} - T\Delta S$, where ΔE_{DFT} is the DFT electronic energy difference of each step, ΔE_{ZPE} and Δ_S are the correction of zero-point energy and the variation of entropy, respectively, which are obtained by vibration analysis, T is the temperature (T =300 K) [30].

3. Results and discussion

3.1. The fabrication of B/CNFs, P-B/CNFs and S-B/CNFs

As proof-of-concept experiments, a series of boron, sulphur and phosphorus doped/co-doped carbon nanofibers with different boron/sulphur/phosphorus contents were successfully designed and synthesized. The typical synthesis procedure of the as-synthesized materials is schematic illustrated in Fig. 1. The H_3BO_3 was firstly dissolved in polymer polyacrylonitrile solution to get homogeneous precursor solution. Then, the PAN/H_3BO_3 nanofiber membrane was obtained through the electrospinning process. Through the graphitization process associated with sulfur vapor or phosphorus vapor treatment, the PAN/H_3BO_3 nanofibers membrane was converted to B-doped carbon nanofibers (B/CNFs), S and B co-doped CNFs (S-B/CNFs), P and B co-doped CNFs (P-B/CNFs), respectively.

3.2. Structural characterization of B/CNFs, P-B/CNFs and S-B/CNFs

The structure and morphology of the as-prepared materials were explored by field emission scanning electron microscope (FE-SEM) and transmission electron microscope (TEM). Fig. S1a shows the FE-SEM image of the as-synthesized B-doped CNFs with B contents of 8.09 at% and the chemical formula of B/CNFs can be inferred as $B_{8.09}$/CNFs. The graphitization temperature is 900 °C. The $B_{8.09}$/CNFs membrane exhibits a three-dimensional network consisted of randomly assembled nanofibers with average diameter of about 200 nm. The inset in Fig. S1a indicates that the contact angle of $B_{8.09}$/CNFs is about 120°, suggesting the hydrophilic surface. High magnification FE-SEM image (Fig. 2a) and TEM image (Fig. 2b) show that the sulphur and boron co-doped CNFs with S and B contents of 6.23 at% and 8.09 at% ($S_{6.23}$-$B_{8.09}$/CNFs) possesses a certain amount of small pores caused by the surface sulphur doping. High resolution TEM image of $S_{6.23}$-$B_{8.09}$/CNFs (inset in Fig. 2b) indicates the distinct graphitized carbon layers and the d spacing distance of visible lattice fringe is 3.6 Å, corresponding to the (002) planes of carbon [31]. The morphology and structure of phosphorus and boron co-doped CNFs with P and B contents of 4.12 at% and 8.09 at% ($P_{4.12}$-$B_{8.09}$/CNFs) were shown in Fig. S1b. The $P_{4.12}$-$B_{8.09}$/CNFs also exhibits the 3D nanofiber networks, and the inset in Fig. S1b demonstrates the hydrophobic surface of $P_{4.12}$-$B_{8.09}$/CNFs with contact angle of 112°. Interestingly, after the S vapor treatment, the as-synthesized $S_{6.23}$-$B_{8.09}$/CNFs (Fig. S1c) exhibits hydrophilic surface, indicating the surface property transformation from hydrophobicity to hydrophilicity triggered by S doping. The results indicate that different doping elements can change the surface property of B/CNFs. The hydrophilicity of $S_{6.23}$-$B_{8.09}$/CNFs is very important for the electrochemical nitrogen reduction reaction (NRR). During the NRR in 0.5 M K_2SO_4 electrolyte, compared with the hydrophobic surface, more potassium ions would absorb and aggregate on the hydrophilic electrode surface. The relatively high concentration of potassium ions on the electrode would strongly retard the migration of protons from the solution to the electrode surface, and therefore, suppress the competitive HER [32].

The high-angle annular dark field scanning transmission electron microscopy (HAADF-STEM) (Fig. 2c) and scanning transmission electron microscopy energy dispersive X-ray spectroscopy (STEM-EDX) mapping (Fig. 2d–f) images of the $S_{6.23}$-$B_{8.09}$/CNFs hybrid demonstrate that the C, B and S elements are uniformly distributed throughout the whole CNFs, suggesting that the S and B were uniformly doped into the CNFs. Fig. 2g displays the electron energy loss spectrum (EELS) of $S_{6.23}$-$B_{8.09}$/CNFs. The fine structure characteristics of π* and σ* are clearly defined by the K edge, suggesting the well-graphitized sp^2 bonded hexagonal network of CNFs [33]. The characteristics of π* for S-K and B-K have confirmed the S and B co-doping in CNFs. Through a systematic quantitative analysis of the chemical composition of the EELS spectrum, it was found that the doping content of B in CNFs was 8.09 at%, while the doping content of S was 6.23 at%.

In order to reveal the composition and crystal structure of the prepared materials, X-Ray diffraction (XRD) patterns were obtained (Fig. 2h). Typical broad diffraction peaks are observed about 22° and 44° for all samples, which are assigned to the (002) and (101) planes of graphitic carbon [34]. Compared with the $B_{8.09}$/CNFs, the (002)

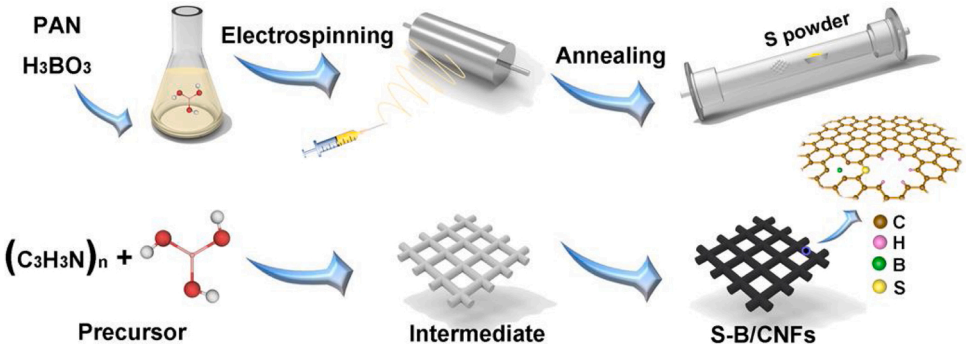

Fig. 1. Schematic illustration of the S-B/CNFs hybrid material synthesis process.

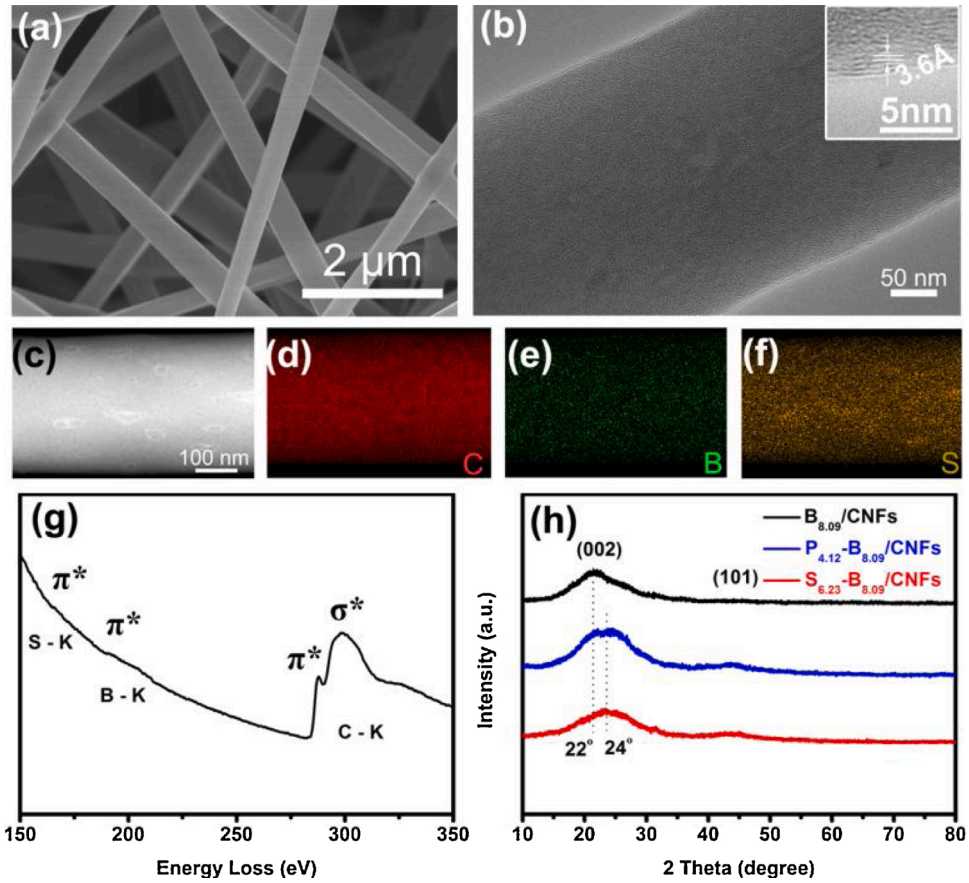

Fig. 2. (a) FE-SEM and (b) TEM image of $S_{6.23}$-$B_{8.09}$/CNFs hybrid and the inset shows the HRTEM image of $S_{6.23}$-$B_{8.09}$/CNFs hybrid. (c-f) HAADF-STEM and STEM-EDX mapping images of $S_{6.23}$-$B_{8.09}$/CNFs hybrid. (g) A typical STEM-EELS spectrum taken from $S_{6.23}$-$B_{8.09}$/CNFs hybrid. (h) XRD patterns of $B_{8.09}$/CNFs, $P_{4.12}$-$B_{8.09}$/CNFs and $S_{6.23}$-$B_{8.09}$/CNFs hybrids.

diffraction peaks of $S_{6.23}$-$B_{8.09}$/CNFs and $P_{4.12}$-$B_{8.09}$/CNFs have slight shifts to higher 2θ and the (101) diffraction peak of $S_{6.23}$-$B_{8.09}$/CNFs and $P_{4.12}$-$B_{8.09}$/CNFs display stronger intensities, indicating the relatively higher graphitization degree due to S, B or P, B co-doping [35].

X-ray photoelectron spectroscopy (XPS) was used to further characterize the chemical states and valence structures of B, S and P atoms in CNFs. All the binding energies (BEs) were calibrated by the C 1s peak at 284.6 eV as reference. The high-resolution B 1s peaks of $B_{8.09}$/CNFs, $P_{4.12}$-$B_{8.09}$/CNFs and $S_{6.23}$-$B_{8.09}$/CNFs are fitted into three peaks (Fig. 3a–c). The BE at 189.9 eV corresponds to the BC_3 bonds, and the formation of BC_3 structures represent the replacement of carbon atoms by boron atoms in the CNF framework [36]. The BEs at 191.2 and 192.3 eV are ascribed to the BC_2O and BCO_2 bonds [37]. The formation of BC_3, BC_2O and BCO_2 structures strongly demonstrate the substitution of B for C atoms at the edges or defects of graphitic carbon [38]. It has been reported that the BC_3 structure in B doped carbon are the active sites for the electrocatalytic NRR [39]. Fig. S2 displays the proportions of BC_3 structures in $S_{6.23}$-$B_{8.09}$/CNFs, $P_{4.12}$-$B_{8.09}$/CNFs and $B_{8.09}$/CNFs hybrids. The $S_{6.23}$-$B_{8.09}$/CNFs exhibits the highest proportion of BC_3 structures (20 %) as compared to those of $B_{8.09}$/CNFs (11 %) and $P_{4.12}$-$B_{8.09}$/CNFs (13 %), indicating that the S doping could induce the formation of BC_3 structures. High-resolution S 2p spectra of the $S_{6.23}$-$B_{8.09}$/CNFs are shown in Fig. 3d. The BEs of three characteristic peaks are located at 163.6 eV, 164.9 eV and 168.0 eV, respectively. The two dominant peaks at 163.6 and 164.9 eV can be assigned to $2p_{3/2}$ and S $2p_{1/2}$ of S orbitals, suggesting that the S atoms only form double bond with C atoms (S═C bonds) [40]. The results strongly confirm the successful doping of S atoms into the carbon framework.

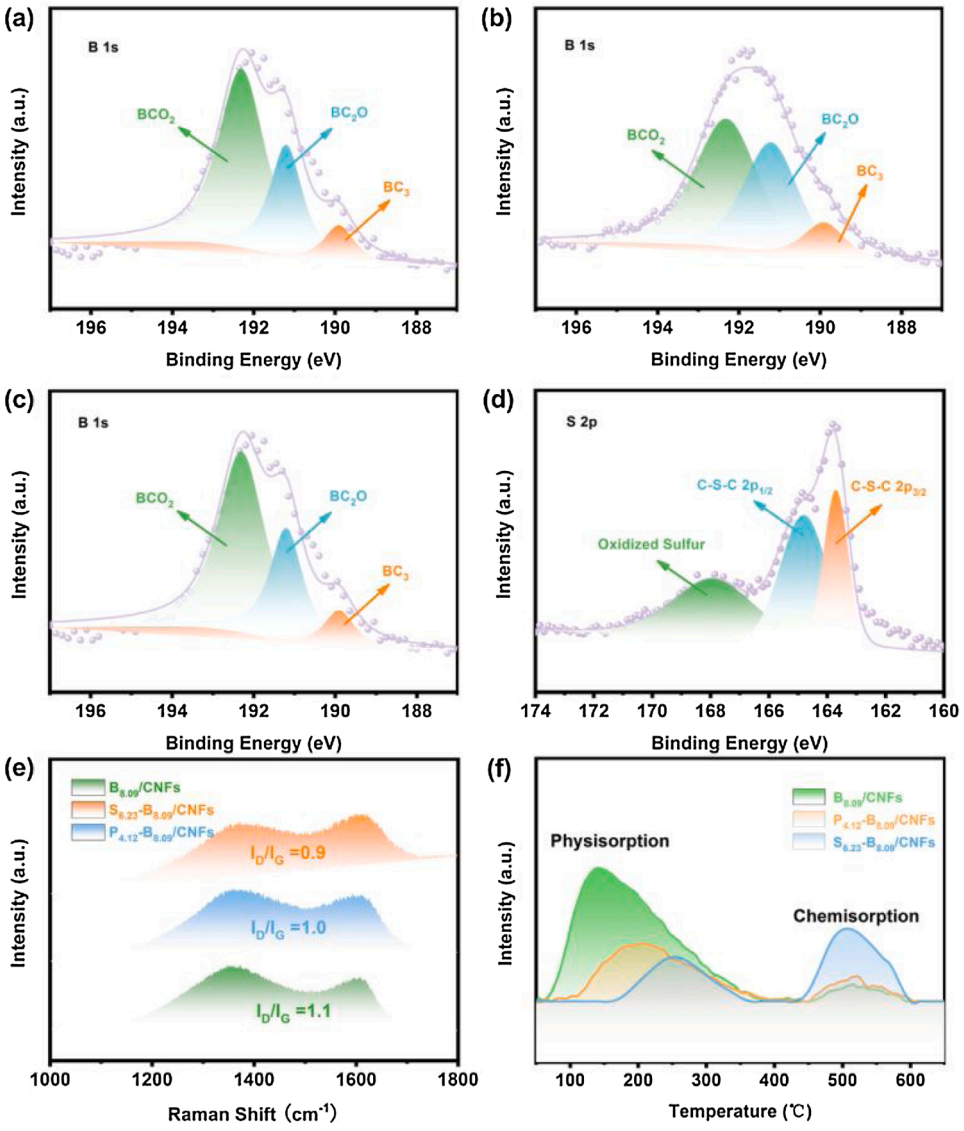

Fig. 3. B 1 s XPS spectra of (a) $B_{8.09}$/CNFs, (b) $P_{4.12}$-$B_{8.09}$/CNFs and (c) $S_{6.23}$-$B_{8.09}$/CNFs hybrids. (d) S 2p XPS spectra of $S_{6.23}$-$B_{8.09}$/CNFs hybrid. (e) Raman spectra of $B_{8.09}$/CNFs, $P_{4.12}$-$B_{8.09}$/CNFs and $S_{6.23}$-$B_{8.09}$/CNFs hybrids. (f) N_2 TPD curves of $B_{8.09}$/CNFs, $P_{4.12}$-$B_{8.09}$/CNFs and $S_{6.23}$-$B_{8.09}$/CNFs hybrids.

Raman spectroscopy was also used to investigate the chemical structures of the samples (Fig. 3e). The characteristic peaks at 1350 and 1590 cm^{-1} correspond to the D and G peaks of the hybrid material, respectively. The ratios of I_D and I_G of $P_{4.12}$-$B_{8.09}$/CNFs, $B_{8.09}$/CNFs and $S_{6.23}$-$B_{8.09}$/CNFs were calculated as 1.0, 1.1 and 0.9 respectively, suggesting that the $S_{6.23}$-$B_{8.09}$/CNFs displays more defect carbon structures due to the substitution of S and B atoms into carbon matrix. Besides the BC_3 structures, these defects in $S_{6.23}$-$B_{8.09}$/CNFs hybrid could also become the new active sites, thereby enhancing the NRR intrinsic activity. The temperature-programmed desorption (TPD) test was used to investigate the ability of as-prepared samples to adsorb N_2 molecule. As shown in Fig. 3f, the peaks at about 140 °C correspond to the physical adsorption of N_2 molecule, and the peaks at about 510 °C attribute to the chemical adsorption of N_2 molecule [41]. It can be seen that the N_2 absorbed on $B_{8.09}$/CNFs are mainly physical adsorption. After the S, B and P, B co-doping, the $P_{4.12}$-$B_{8.09}$/CNFs and $S_{6.23}$-$B_{8.09}$/CNFs hybrids display the significantly enhanced chemical adsorption of N_2 molecule, indicating that the secondary doping by S and P could improve the chemical absorption ability for N_2 on B/CNFs surfaces. The TPD results indicate that the $S_{6.23}$-$B_{8.09}$/CNFs has the strongest chemisorption ability of N_2 molecule, suggesting the highest activity for NRR.

3.3. Electrochemical evaluation of B/CNFs, P-B/CNFs and S-B/CNFs for NRR

The electrochemical NRR activity of all the as-prepared samples was performed in N_2-saturated 0.5 M K_2SO_4 solution using an H-type electrochemical cell (Fig. 4a). The photograph of H-type electrochemical setup was shown in Fig. S3. The Ag/AgCl reference electrode was placed in the cathode chamber. The platinum wire used as counter electrode was placed in the anode chamber. Before the performance test, the N_2 pretreated with acid solution was blown into the cathode chamber. The Faraday efficiency (FE) and ammonia yield were calculated from the ultraviolet-visible spectrum. The polarization curves of $B_{8.09}$/CNFs, $P_{4.12}$-$B_{8.09}$/CNFs and $S_{6.23}$-$B_{8.09}$/CNFs hybrids were obtained in N_2 saturated electrolytes (Fig. S4). The as synthesized samples exhibit different current densities with potential ranged from -0.6 V ~ -0.8 V vs RHE, indicative of a N_2 reduction event. In addition, the potential below -0.8 V vs RHE is a favorable area for HER. Among all the samples, the $S_{6.23}$-$B_{8.09}$/CNFs exhibits the best NRR activity than the $B_{8.09}$/CNFs and $P_{4.12}$-$B_{8.09}$/CNFs hybrids.

In order to investigate the effects of B, S, and P doping in CNFs on the NRR activity, we firstly designed a series of B/CNFs with different B

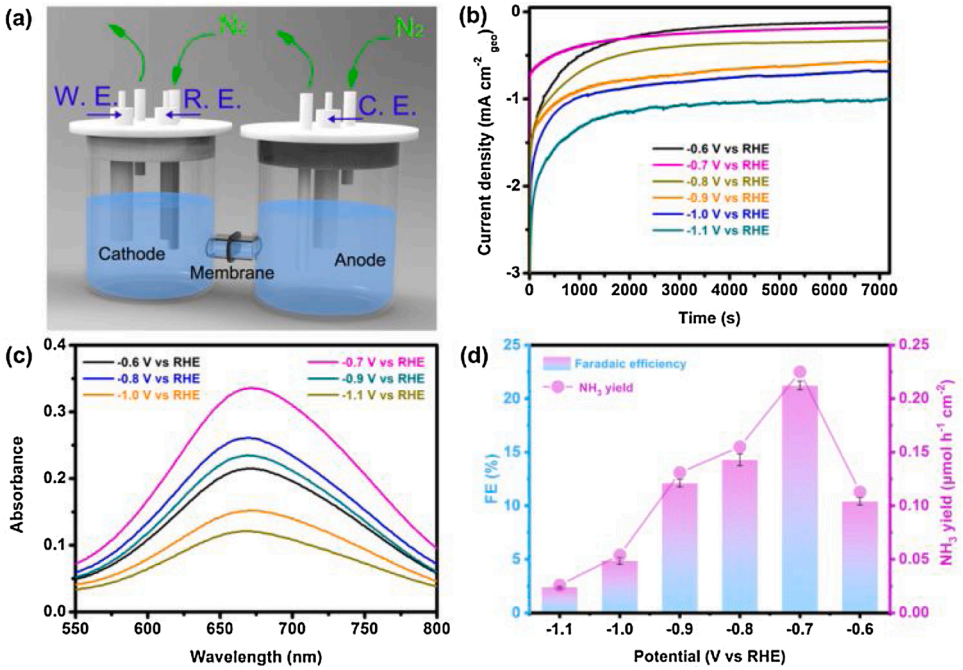

Fig. 4. (a) Schematic diagram of the electrochemical cell used for NRR. (b) Chronoamperometry curves of of $S_{6.23}$-$B_{8.09}$/CNFs at various potentials for 2 h in N_2-saturated 0.5 M K_2SO_4. (c) The UV–vis absorbance spectra of ammonia production for $S_{6.23}$-$B_{8.09}$/CNFs at various potentials in N_2-saturated 0.5 M K_2SO_4. (d) The Faradaic efficiency and the corresponding NH_3 yield for $S_{6.23}$-$B_{8.09}$/CNFs at various potentials in N_2-saturated 0.5 M K_2SO_4.

contents and the surface atomic ratios were measured by the energy dispersive X-ray spectra (EDS). The atomic ratios of B in CNFs are 3.10, 4.84, 6.87, 8.09 and 9.09 at%, respectively and the chemical formula can be inferred as $B_{3.10}$/CNFs, $B_{4.84}$/CNFs, $B_{6.87}$/CNFs, $B_{8.09}$/CNFs and $B_{9.09}$/CNFs, respectively. In addition, the pure CNFs exhibit negligible NRR activity, indicating that the carbon did not have the intrinsic activity for NRR without B doping (Fig. S5). Fig. S6a shows the UV–vis absorption spectra of different B/CNFs with various B contents in CNFs. Under increased work potentials and current density outputs, the $B_{8.09}$/CNFs obtains the highest Faradaic efficiency (FE) for NH_3 of 9.7 % and NH_3 yields of 0.097 μmol h^{-1} cm^{-2} at -0.7 V vs RHE in 0.5 M K_2SO_4 electrolyte, respectively (Fig. S6b). Interestingly, the FE and NH_3 yield change with the different B contents in CNFs. The FE and NH_3 yield increase with the increased B contents from 3.10 to 8.09 at%. However, the $B_{9.09}$/CNFs with highest B content of 9.09 at% exhibits a significant decrease in FE and NH_3 yield when compared with $B_{8.09}$/CNFs. It is because that the NRR is surface reaction and the BC_3 structures on the surfaces of B/CNFs are mainly the active sites, involving in the NRR. Meanwhile, the B elements are uniformly distributed throughout the whole CNFs and BC_3 in the inner of CNFs cannot be the active sites for NRR. Therefore, the 8.09 at% is the ideal B contents in $B_{8.09}$/CNFs for NRR.

The influences of graphitization temperature on the NRR activity were also investigated. The UV–vis absorption spectra of B/CNFs prepared at different graphitization temperatures from 800 to 1000 °C were shown in the Fig. S7a. The $B_{8.09}$/CNFs prepared at 800, 900 and 1000 °C display quite different absorption spectra. As shown in Fig. S7b, after the continuous NRR electrolysis for 2 h, the $B_{8.09}$/CNFs-900 obtains the highest FE of 9.7 % for NH_3 and the NH_3 yield of 0.097 μmol h^{-1} cm^{-2} at -0.7 V vs RHE in 0.5 M K_2SO_4 electrolyte. The B contents of the B/CNFs prepared at 800, 900 and 1000 °C are 5.04, 8.09 and 6.52 at%, respectively. The variation trends of B content change caused by the graphitization temperature are according with the trends of NRR activity. The various graphitization temperatures lead to the changing of B contents in B/CNFs and meanwhile influence the NRR activity. The preparations of P-B/CNFs and S-B/CNFs hybrids were performed at the optimal graphitization temperature of 900 °C to insure the ideal B content.

In order to show the effects of doping with secondary elements on the NRR activity of B/CNFs, we have designed a series of P-B/CNFs and S-B/CNFs hybrids prepared at 900 °C. The UV–vis spectra of a series of P-B/CNFs with different P contents are shown in Fig. S8a. The $P_{4.12}$-$B_{8.09}$/CNFs obtains the strongest absorption intensity. After the continuous NRR electrolysis for 2 h, Fig. S8b shows that the $P_{4.12}$-$B_{8.09}$/CNFs acquires the highest FE of 13.2 % for NH_3 and ammonia yield of 0.132 μmol h^{-1} cm^{-2} at -0.7 V vs RHE in 0.5 M K_2SO_4 electrolyte. The results indicate that the P-B/CNFs with P contents of 4.12 at% and B content of 8.09 at% exhibit the highest NRR activity.

Similarly, the S contents of S-B/CNFs hybrids also influence the NRR activity. The UV–vis spectra of S-B/CNFs prepared at different S contents are shown in Fig. S9a. The $S_{6.23}$-$B_{8.09}$/CNFs exhibits the highest FE of 22.4 % for NH_3 and ammonia yield of 0.223 μmol h^{-1} cm^{-2} at -0.7 V vs RHE in 0.5 M K_2SO_4 electrolyte (Fig. S9b). The results indicate that with the ideal B content in CNFs, the contents of the secondary P or S elements have significant influences on the NRR activity. In comparison, the $S_{6.23}$-$B_{8.09}$/CNFs exhibits the higher FE and ammonia yield than $P_{4.12}$-$B_{8.09}$/CNFs.

The chronoamperometry curves of $S_{6.23}$-$B_{8.09}$/CNFs obtained at various potentials are shown in Fig. 4b. The current density keeps stable in 2 h and high potentials lead to the increasing in the current densities. The electrolyte after continuous electrolysis for 2 h was characterized *via* the UV–vis spectroscopy by colorimetry. The UV–vis absorbance curve spectra of $S_{6.23}$-$B_{8.09}$/CNFs performed at various potentials are shown in Fig. 4c. Under increased work potential, the $S_{6.23}$-$B_{8.09}$/CNFs obtains the highest FE of about 22.4 % and ammonia yield of about 0.223 μmol h^{-1} cm^{-2} at -0.7 V vs RHE in 0.5 M K_2SO_4 electrolyte (Fig. 4d), which is highly comparable to that of reported state-of-the-art NRR electrocatalysts (Table S1, Supporting Information). The contents of by-product N_2H_4 were determined by the Watt-Christo method. Fig. S10 shows the UV–vis absorption spectra of the electrolyte mixed with p-$C_9H_{11}NO$ indicator after NRR electrolysis at various potentials. Figs. S11-12 shows the UV-vis absorption spectra of the various NH_4^+ ions and various N_2H_4 concentration. The absence of N_2H_4 indicates that the NRR reaction on $S_{6.23}$-$B_{8.09}$/CNFs shows a good selectivity for NH_3 synthesis.

Furthermore, the stability is vital for practical application. Fig. 5a displays the continuous 10-time cycles of $S_{6.23}$-$B_{8.09}$/CNFs for NRR performed at -0.7 V vs RHE in 0.5 M K_2SO_4 electrolyte. The FE for NH_3 and the NH_3 yield both keep stable during the continuous 10-time cycles. There was no obvious reduction in the FE and NH_3 yield, which indicate the excellent repeatability of $S_{6.23}$-$B_{8.09}$/CNFs. To further confirm the durability of $S_{6.23}$-$B_{8.09}$/CNFs hybrid, the long-term time dependent current density curves for continuous NRR electrolysis was obtained (Fig. 5b). There is negligible decrease in the current density during the continuous NRR electrolysis for 10 h. Fig. S13a and b showed the FE-SEM, TEM and HRTEM images of the $S_{6.23}$-$B_{8.09}$/CNFs after 10 h electrochemical stability test, suggesting that the morphology of the one-dimensional fibers remained the same when compared with the pristine catalyst. In addition, there were no obvious changes in the B 1 s XPS spectra after the NRR (Fig. S13c). The BC_3 structure still existed in the $S_{6.23}$-$B_{8.09}$/CNFs. High-resolution S 2p spectrum of the $S_{6.23}$-$B_{8.09}$/CNFs was shown in Fig. S13d after 10 h electrochemical stability test, and the results suggested that the S atoms were firmly embedded in the carbon framework. Therefore, the excellent morphology and chemical states of $S_{6.23}$-$B_{8.09}$/CNFs after long-term NRR tests demonstrated the superior stability. Meanwhile, to reveal the importance of nitrogen molecules evolved in the NRR process, the electrochemical NRR tests were performed at -0.7 V vs RHE by alternating the N_2-saturated and Ar-saturated electrolytes (Fig. 5c). It is shown that the NH_3 only produced when the N_2 involved in the electrolyte. Otherwise, under the Ar condition, there is almost no NH_3 produced and detected in the electrolyte. In order to confirm the N source of NH_3 production, the UV–vis spectroscopies of the original K_2SO_4 solution, the N_2-saturated and Ar-saturated K_2SO_4 solutions were collected at -0.7 V, and the UV–vis spectroscopies of N_2-saturated K_2SO_4 solution was collected at open circuit potential. As shown in Fig. 5e, NH_3 is only obviously generated at -0.7 V vs RHE in N_2-saturated K_2SO_4 solution. The FE and NH_3 yield of $S_{6.23}$-$B_{8.09}$/CNFs are 22.4 % and 0.023 μmol h^{-1} cm^{-2} (Fig. 5d), respectively. The Ar-saturated K_2SO_4 solution performed at a -0.7 V and the N_2-saturated electrolyte performed at open circuit voltage both display negligible NH_3 yields. In addition, to further confirm the source of ammonia, ^{15}N isotope labelling experiments were used to exhibit that the ammonia product in the electrolyte was completely originated from the feeding N_2. As shown in Fig. 5f, the $^{14}N_2$-saturated K_2SO_4 solution performed at -0.7 V vs RHE exhibits a triplet coupling (52 Hz) for $^{14}NH_4^+$. After NRR electrolysis using $^{15}N_2$ as feeding gas, a doublet pattern with the coupling constant of $J_{N\text{-}H}$ =72 Hz was detected, corresponded to $^{15}NH_4^+$ in the acidic solution. The above results indicate that the detected NH_3 products are originated from the N_2 through the NRR process catalyzed by $S_{6.23}$-$B_{8.09}$/CNFs hybrid.

The electrochemical NRR results indicate that with the secondary element co-doping, the S-B/CNFs and P-B/CNFs both exhibit enhanced NRR activity. In addition, the doping contents of S, P and B in CNFs play an important role in improving the FE and NH_3 yield. Among the series of designed electrocatalysts, the $S_{6.23}$-$B_{8.09}$/CNFs with S and B contens of 6.23 and 8.09 at% shows the highest NRR activity with a NH_3 yield of 0.223 μmol h^{-1} cm^{-2} and a Faradaic efficiency of 22.4 %, suggesting that the NRR activity can be easily adjusted.

3.4. Theory-guided calculations

In order to investigate the reaction pathways and the mechanism of the excellent NRR activity on $S_{6.23}$-$B_{8.09}$/CNFs hybrid, the density

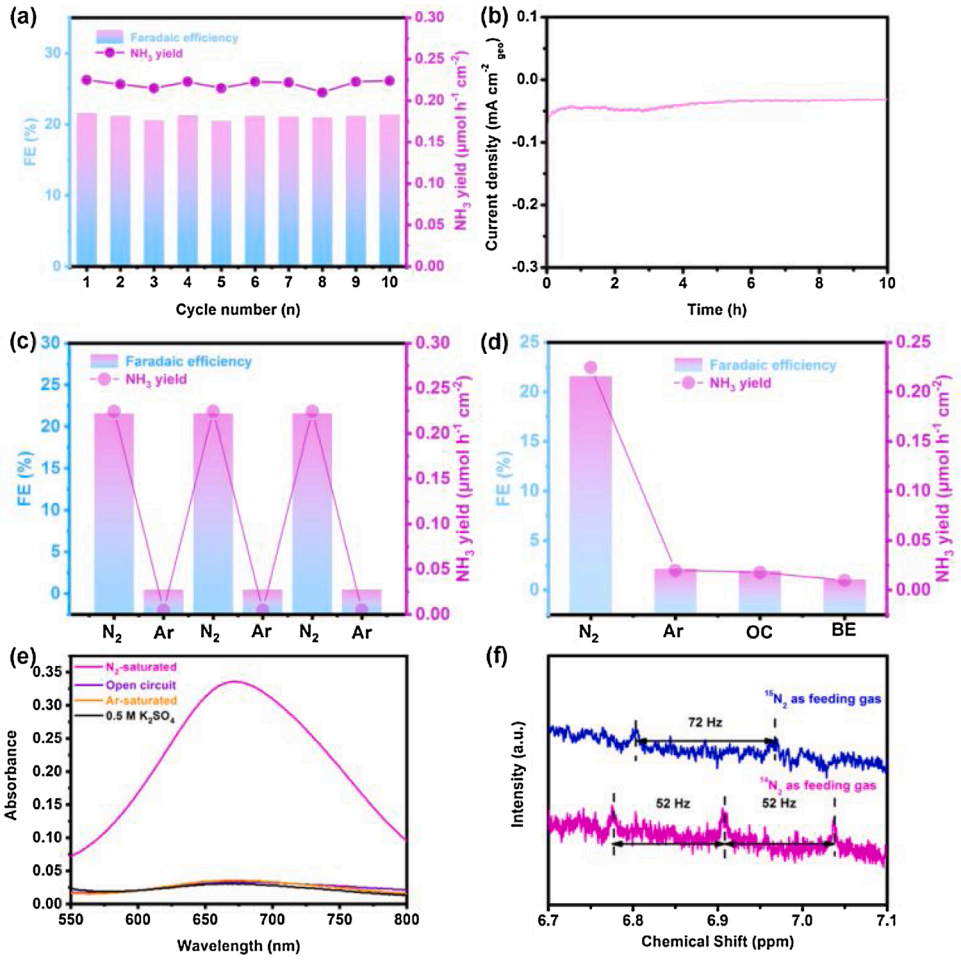

Fig. 5. (a) The NH_3 yield and the corresponding FE for NH_3 of $S_{6.23}$-$B_{8.09}$/CNFs obtained at -0.7 V vs RHE during 10-time cycles for NRR in N_2-saturated 0.5 M K_2SO_4. (b) Time-dependent current density curve of $S_{6.23}$-$B_{8.09}$/CNFs performed at -0.7 V vs RHE for 10 h in N_2-saturated 0.5 M K_2SO_4. (c) The FE and the corresponding NH_3 yield of $S_{6.23}$-$B_{8.09}$/CNFs performed at -0.7 V vs RHE by alternating Ar-saturated and N_2-saturated 0.5 M K_2SO_4. (d) The FE and the corresponding NH_3 yield of $S_{6.23}$-$B_{8.09}$/CNFs obtained at -0.7 V vs RHE in N_2-saturated 0.5 M K_2SO_4, 0.5 M K_2SO_4 (BE) and Ar-saturated 0.5 M K_2SO_4, and at open circuit (OC) in N_2-saturated 0.5 M K_2SO_4. (e) UV–vis absorption spectra of under N_2-saturated 0.5 M K_2SO_4, 0.5 M K_2SO_4 (BE) and Ar-saturated 0.5 M K_2SO_4, and at open circuit (OC) in N_2-saturated 0.5 M K_2SO_4 of $S_{6.23}$-$B_{8.09}$/CNFs hybrid. (f) The ^1H NMR spectra of obtained at -0.7 V vs RHE in 0.5 M K_2SO_4 of $S_{6.23}$-$B_{8.09}$/CNFs hybrid using $^{14}N_2$ or $^{15}N_2$ as the nitrogen source.

functional theory (DFT) calculations were used to explore the p-band center of B and map out the energy profile of NRR on $S_{6.23}$-$B_{8.09}$/CNFs. The above XPS results in Fig. 2 demonstrate that in the chemical structures of $S_{6.23}$-$B_{8.09}$/CNFs, the S can only form double bond with C, and therefore, the S atom can be only formed at the edge of carbon framework. According to the literatures, the BC_3 structures in B-doped carbon materials are the main active sites for NRR. In this work, the introduce of S atoms into B doped carbon structures would lead to the localized electron distribution and charge transformation, which are the key factors in determining the NRR activity [42]. As shown in Fig. 6a, based on the experimental data, we constructed three kinds of S, B co-doping carbon framework with different B atom positions for calculation and simulation. Due to the different position of B atoms, the obtained models are correspondingly named as B/CNFs, 1-S-B/CNFs, 2-S-B/CNFs and 3-S-B/CNFs (Figs. S14−17).

The B-based metal-free catalysts usually follow the proton-electron coupling remote association pathway [43]. The adsorption of N_2 on the active center is a vital step and the first step of hydrogenation is considered to be the rate-determining step in this pathway [44]. Therefore, We propose an associative pathway of S-B/CNFs, in which N_2→*NN and *NN→*NNH are the two main rate-determining steps. We firstly compared the adsorption energies of N_2 molecule on these four models. As shown in Fig. 6b, the strong N_2 fixation capacity makes the 2-S-B/CNFs easily tended to activate N_2 into $*N_2$ intermediates with energy barrier as low as 0.18 eV. In comparison, as shown in Figs. S18−20, the B/CNFs, 1-S-B/CNFs and 3-S-B/CNFs require higher N_2 adsorption energy barriers of 0.41, 0.30 and 0.41 eV, respectively, suggesting the weaker adsorptions of N_2 molecules. The results indicate that introduce of S atoms into BC_3 structures make parts of the BC_3 more active for absorbing N_2 molecules with a lower energy barrier (0.18 eV) when compared with the pure BC_3 sites (0.41 eV). In addition, due to the higher electronegativity (2.58) than C (2.55) and B (2.04), the S atoms can be used as electron donors source to enhance the adsorption of N_2 on S-C-B sites, leading to more stable B-N_2 interactions and enhanced NRR intrinsic activity [45].

In addition, the formation energy of the adsorbed intermediate *NNH is the central rate-determining step in NRR [46]. The formation energy for *NNH on 2-S-B/CNFs is 2.07 eV (Fig. 6b). Figs. S18−20 indicate that the formation energy for *NNH on B/CNFs, 1-S-B/CNFs and 3-S-B/CNFs are 2.30, 2.31 and 2.35 eV, respectively, suggesting that 2-S-B/CNFs shows the lowest energy barrier for the generation of *NNH intermediates. Herein, comparing the free energy of each intermediate products ($*NNH_2$, *N, *NH, $*NH_2$ and $*NH_3$) in the NRR pathway, the relatively low energy barrier in the rate-determining steps on the S-C-B active sites predicts that $S_{6.23}$-$B_{8.09}$/CNFs is an excellent catalyst toward NRR. Moreover, according to the *p*-band center theory, the catalytic active of non-metal elements are related to the central position of the p_z orbital [47]. Therefore, as shown in the Fig. 6c, we have also plotted the proposed partial density of states of B atoms in 2-S-B/CNFs model. The p_z orbital center position of B in 2-S-B/CNFs located at -4.36 eV. Figs. S21−23 show the p_z orbital center positions of B in B/CNFs (-3.22 eV), 1-S-B/CNFs (-4.26 eV) and 3-S-B/CNFs (-4.21 eV). The results demonstrate that the p_z orbital center position of B in 2-S-B/CNFs (-4.36 eV) moves to high energy which is far from the Fermi level (0 eV). In addition, to understand the effects of S, B dopants in CNFs on the HER activity, the Gibbs free energy of hydrogen adsorption were also calculated (Fig. S24). It reveals that the B active sites of B/CNFs and 2-S-B/CNFs models have similar hydrogen adsorption capability (1.14 vs 1.13 eV). However, the S active sites of 2-S-B/CNFs model possess weaker hydrogen adsorption capability (1.95 eV). Therefore, the introduction of S sites in 2-S-B/CNFs models would inhibit the HER, suggesting that the S, B co-doped CNFs exhibit enhanced NRR performance. Through the above reaction pathways and free energy analysis, the 2-S-B/CNFs model possesses the ideal NRR performance. The DFT simulation results match well with the experimental data. The doping of S atoms into BC_3 structures not only reduce the energy barriers for rate-determining steps for NRR, but also make the center of the p_z orbital of B moved to high energy and are far away from the Fermi level, leading to the superior NRR intrinsic activity.

4. Conclusion

In summary, we employed CNFs as host and nanoreactor to synthesize a series of boron, sulphur or boron, sulphur co-doped carbon materials and the B, S and P contents in CNFs can be controlled well. The well-defined $S_{6.23}$-$B_{8.09}$/CNFs displayed outstanding NRR performance

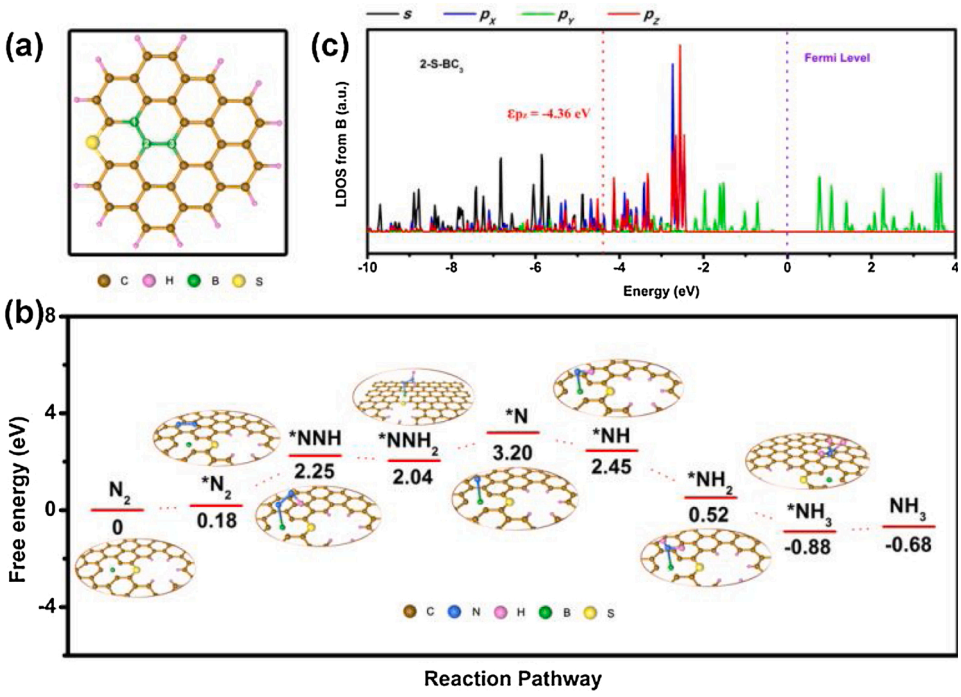

Fig. 6. (a) The model of S, B co-doped CNFs with different B atom positions. (b) Calculated free energy profiles (ΔG) for NRR reaction pathway on 2-S-B/CNFs structure. The structures of reaction intermediates are shown next to their energy segments. (c) Local Density of states (LDOS) plots of B atoms in 2-S-B/CNFs hybrid system. The colored solid lines show the projected DOS from s, p_x, p_y and p_z orbitals, respectively. The red dashed lines and the numbers next to them indicate the B p_z band centers for system.

with high NH_3 yield of 0.223 μmol h^{-1} cm^{-2} and Faradaic efficiency of 22.4 % at −0.7 V versus reversible hydrogen electrode in 0.5 M K_2SO_4, which is superior to those of $B_{8.09}$/CNFs and $P_{4.12}$-$B_{8.09}$/CNFs hybrids. We revealed that the heteroatom-doping of S atoms induced changing of center position of the p_z orbital of B facilitates the adsorption of N_2 on S-C-B sites and reduces the energy barriers for rate-determining step of the first protonation to form *NNH. The combined computational and experimental work uncovers the relationship between the *p*-band center of heteroatom doped carbon catalysts and NRR activity and paves a way for their future application.

CRediT authorship contribution statement

Yankun Wen: Conceptualization, Methodology, Formal analysis, Writing - original draft. **Han Zhu:** Project administration, Formal analysis, Validation, Writing - review & editing, Supervision, Funding acquisition. **Jiace Hao:** Resources, Investigation. **Shuanglong Lu:** Resources, Writing - review & editing. **Wei Zong:** Formal analysis. **Feili Lai:** Formal analysis, Supervision. **Piming Ma:** Project administration. **Weifu Dong:** Project administration. **Tianxi Liu:** Formal analysis, Supervision. **Mingliang Du:** Supervision, Funding acquisition.

Declaration of Competing Interest

The authors report no declarations of interest.

Acknowledgements

This study is supported by the National Natural Science Foundation of China (NSFC) (Grant nos. 52073124, 51803077), Natural Science Foundation of Jiangsu Province (Grant nos. BK20180627), Postdoctoral Science Foundation of China (2018M630517, 2019T120389), the MOE & SAFEA, 111 Project (B13025), the national first-class discipline program of Light Industry Technology and Engineering (LITE2018-19), and the Fundamental Research Funds for the Central Universities. We also thank the characterizations supported by Central Laboratory, School of Chemical and Material Engineering, Jiangnan University.

References

[1] J.W. Erisman, M.A. Sutton, J. Galloway, Z. Klimont, W. Winiwarter, How a century of ammonia synthesis changed the world, Nat. Geosci. 1 (2008) 636–639.
[2] M.A. Légaré, G. Bélanger-Chabot, R.D. Dewhurst, E. Welz, I. Krummenacher, B. Engels, H. Braunschweig, Nitrogen fixation and reduction at boron, Science 359 (2018) 896–900.
[3] T. Wang, S.X. Li, B.L. He, X.J. Zhu, Y.L. Luo, Q. Liu, T.S. Li, S.Y. Lu, C. Ye, A. M. Asiri, X.P. Sun, Commercial indium-tin oxide glass: a catalyst electrode for efficient N_2 reduction at ambient conditions, Chin. J. Catal. 42 (2020) 1024–1029.
[4] W.B. Qiu, X.Y. Xie, J.D. Qiu, W.H. Fang, R.P. Liang, X. Ren, X.Q. Ji, G.W. Cui, A. M. Asiri, G.L. Cui, B. Tang, X.P. Sun, High-performance artificial nitrogen fixation at ambient conditions using a metal-free electrocatalyst, Nat. Commun. 9 (2018) 1–8.
[5] K. Chu, Q.Q. Li, Y.P. Liu, J. Wang, Y.H. Cheng, Filling the nitrogen vacancies with sulphur dopants in graphitic C_3N_4 for efficient and robust electrocatalytic nitrogen reduction, Appl. Catal. B: Environ. 267 (2020), 118693.
[6] T. Xu, B.Y. Ma, J. Liang, L.C. Yue, Q. Liu, T.S. Li, H.T. Zhao, Y.L. Luo, S.Y. Lu, X. P. Sun, Recent progress in metal-free electrocatalysts toward ambient N_2 reduction reaction, Acta Phys. -Chim. Sin. 37 (2021), 2009043.
[7] A.S. Fajardo, P. Westerhoff, C.M. Sanchez-Sanchez, S. Garcia-Segura, Earth-abundant elements a sustainable solution for electrocatalytic reduction of nitrate, Appl. Catal. B: Environ. 281 (2021), 119465.
[8] T.W. Wu, H.T. Zhao, X.J. Zhu, Z. Xing, Q. Liu, T. Liu, S.Y. Gao, S.Y. Lu, G. Chen, A. M. Asiri, Y.N. Zhang, X.P. Sun, Identifying the origin of Ti^{3+} activity toward enhanced electrocatalytic N_2 reduction over TiO_2 nanoparticle modulated by mixed-valent copper, Adv. Mater. 32 (2020), 2000299.
[9] B. Liu, Y.P. Zheng, H.Q. Peng, B.F. Ji, Y. Yang, Y.B. Tang, C.S. Lee, W.J. Zhang, Nanostructured and boron-doped diamond as an electrocatalyst for nitrogen fixation, ACS Energy Lett. 5 (2020) 2590–2596.
[10] C. Guo, X. Liu, L. Gao, X. Kuang, X. Ren, X.J. Ma, M.Z. Zhao, H. Yang, X. Sun, Q. Wei, Fe-doped Ni_2P nanosheets with porous structure for electroreduction of nitrogen to ammonia under ambient conditions, Appl. Catal. B: Environ. 263 (2020), 118296.
[11] R.B. Zhao, Q. Geng, L. Chang, P.P. Wei, Y.L. Luo, X.F. Shi, A.M. Asiri, S.Y. Lu, Z. M. Wang, X.P. Sun, Cu_3P nanoparticles-reduced graphene oxide hybrid: an efficient electrocatalyst to realize N_2-to-NH_3 conversion under ambient conditions, Chem. Commun. 56 (2020) 9328–9331.
[12] T. Wang, Q. Liu, T.S. Li, S.Y. Lu, G. Chen, X.F. Shi, A.M. Asiri, Y.L. Luo, D.W. Ma, X. P. Sun, Magnetron sputtered Mo_3Si thin film: an efficient electrocatalyst for N_2 reduction at ambient conditions, J. Mater. Chem. A 9 (2021) 884–888.
[13] L. Zhang, X.Q. Ji, X. Ren, Y.J. Ma, X.F. Shi, Z.Q. Tian, A.M. Asiri, L. Chen, B. Tang, X.P. Sun, Electrochemical ammonia synthesis via nitrogen reduction reaction on a MoS_2 catalyst: theoretical and experimental studies, Adv. Mater. 30 (2018), 1800191.
[14] K. Chu, Y.P. Liu, Y.B. Li, H. Zhang, Y. Tian, Efficient electrocatalytic N_2 reduction on CoO quantum dots, J. Mater. Chem. A 7 (2019) 4389–4394.
[15] J.J. Gao, X. Lv, F.Y. Wang, Y.S. Luo, S.Y. Lu, G. Chen, S.Y. Gao, B.H. Zhong, X. D. Guo, X.P. Sun, Enabling electrochemical conversion of N_2 to NH_3 at ambient conditions by CoP_3 nanoneedle array, J. Mater. Chem. A 8 (2020) 17956–17959.
[16] K. Chu, Y.H. Cheng, Q.Q. Li, Y.P. Liu, Y. Tian, Fe-doping induced morphological changes, oxygen vacancies and Ce^{3+}-Ce^{3+} pairs in CeO_2 for promoting electrocatalytic nitrogen fixation, J. Mater. Chem. A 8 (2020) 5865–5873.
[17] B.Y. Ma, J. Liang, T.S. Li, Q. Liu, Y.S. Luo, S.Y. Lu, A.M. Asiri, D.W. Ma, X.P. Sun, Iron-group electrocatalysts for ambient nitrogen reduction reaction in aqueous media, Nano Res. 14 (2021) 555–569.
[18] Y.Y. Yang, L.F. Zhang, Z.P. Hu, Y. Zheng, C. Tang, P. Chen, R.G. Wang, K.W. Qiu, J. Mao, S.Z. Qiao, The crucial role of charge accumulation and spin polarization in activating carbon-based catalysts for electrocatalytic nitrogen reduction, Angew. Chem. Int. Ed. 59 (2020) 4525–4531.
[19] P.P. Wei, Q. Geng, A.I. Channa, X. Tong, Y.S. Luo, S.Y. Lu, G. Chen, S.Y. Gao, Z. M. Wang, X.P. Sun, Electrocatalytic N_2 reduction to NH_3 with high Faradaic efficiency enabled by vanadium phosphide nanoparticle on V foil, Nano Res. 13 (2020) 2967–2972.
[20] K. Chu, Y.P. Liu, Y.B. Li, Y.L. Guo, Y. Tian, Two-dimensional (2D)/2D interface engineering of a MoS_2/C_3N_4 heterostructure for promoted electrocatalytic nitrogen fixation, ACS Appl. Mater. Interfaces 12 (2020) 7081–7090.
[21] X. Cheng, J.W. Wang, W. Xiong, T. Wang, T.W. Wu, S.Y. Lu, G. Chen, S.Y. Gao, X. F. Shi, Z.J. Jiang, X.B. Niu, X.P. Sun, Greatly enhanced electrocatalytic N_2 reduction over V_2O_3/C by P doping, ChemNanoMat 6 (2020) 1315–1319.
[22] K. Chu, Y.P. Liu, Y.H. Cheng, Q.Q. Li, Synergistic boron-dopants and boron-induced oxygen vacancies in MnO_2 nanosheets to promote electrocatalytic nitrogen reduction, J. Mater. Chem. A 8 (2020) 5200–5208.
[23] X. Liu, Y. Jiao, Y. Zheng, S.Z. Qiao, Isolated boron sites for electroreduction of dinitrogen to ammonia, ACS Catal. 10 (2020) 1847–1854.
[24] W. Pei, S. Zhou, Y. Bai, J.J. Zhao, N-doped graphitic carbon materials hybridized with transition metals (compounds) for hydrogen evolution reaction: understanding the synergistic effect from atomistic level, Carbon 133 (2018) 260–266.
[25] D. Zhu, L. Zhang, R.E. Ruther, R.J. Hamers, Photo-illuminated diamond as a solid-state source of solvated electrons in water for nitrogen reduction, Nat. Mater. 12 (2013) 836–841.
[26] G.W. Watt, J.D. Chrisp, Spectrophotometric method for determination of hydrazine, Anal. Chem. 24 (1952) 2006–2008.
[27] G. Kresse, J. Furthmüller, Efficiency of ab-initio total energy calculations for metals and semiconductors using a plane-wave basis set, Comput. Mater. Sci. 6 (1996) 15–50.
[28] P.E. Blöchl, Projector augmented-wave method, Phys. Rev. B 50 (1994) 17953.
[29] J.P. Perdew, J.A. Chevary, S.H. Vosko, M.R. Pederson, D.J. Singh, C. Fiolhais, Atoms, molecules, solids, and surfaces: applications of the generalized gradient approximation for exchange and correlation, Phys. Rev. B 46 (1992) 6671.
[30] E. Skulason, T. Bligaard, S. Gudmundsdóttir, F. Studt, J. Rossmeisl, F. Abild-Pedersen, T. Vegge, H. Jónsson, J.K. Nørskov, A theoretical evaluation of possible transition metal electro-catalysts for N_2 reduction, Phys. Chem. Chem. Phys. 14 (2012) 1235–1245.
[31] H. Tabassum, R.Q. Zou, A. Mahmood, Z.B. Liang, S.J. Guo, A catalyst-free synthesis of B, N co-doped graphene nanostructures with tunable dimensions as highly efficient metal free dual electrocatalysts, J. Mater. Chem. A 4 (2016) 16469–16475.
[32] Y.C. Hao, Y. Guo, L.W. Chen, M. Shu, X.Y. Wang, T.A. Bu, W.Y. Gao, N. Zhang, X. Su, X. Feng, J.W. Zhou, B. Wang, C.W. Hu, A.X. Yin, R. Si, Y.W. Zhang, C.H. Yan, Promoting nitrogen electroreduction to ammonia with bismuth nanocrystals and potassium cations in water, Nat. Catal. 2 (2019) 448–456.
[33] Z. Xu, W.G. Lu, W.L. Wang, C.Z. Gu, K.H. Liu, X.D. Bai, E.G. Wang, H.J. Dai, Converting metallic single-walled carbon nanotubes into semiconductors by boron/nitrogen co-doping, Adv. Mater. 20 (2008) 3615–3619.
[34] B. Chang, L.L. l, D. Shi, H.H. Jiang, Z.Z. Ai, S.Z. Wang, Y.L. Shao, J.X. Shen, Y. Z. Wu, Y.L. Li, X.P. Hao, Metal-free boron carbonitride with tunable boron lewis acid sites for enhanced nitrogen electroreduction to ammonia, Appl. Catal. B: Environ. 283 (2021), 119622.
[35] H. Tabassum, C. Qu, K.T. Cai, W. Aftab, Z.B. Liang, T.J. Qiu, A. Mahmood, W. Meng, R.Q. Zou, Large-scale fabrication of BCN nanotube architecture entangled on a three-dimensional carbon skeleton for energy storage, J. Mater. Chem. A 6 (2018) 21225–21230.
[36] B.N. Yun, H.L. Du, J.Y. Hwang, H.G. Jung, Y.K. Sun, Improved electrochemical performance of boron-doped carbon-coated lithium titanate as an anode material for sodium-ion batteries, J. Mater. Chem. A 5 (2017) 2802–2810.
[37] Y.H. Yu, S.X. Yang, M.L. Dou, Z.P. Zhang, F. Wang, Photochemically activated atomic ruthenium supported on boron-doped carbon as a robust electrocatalyst for hydrogen evolution, J. Mater. Chem. A 8 (2020) 16669–16675.
[38] Y. Kong, Y. Li, B. Yang, Z.J. Li, Y. Yao, J.G. Lu, L.C. Lei, Z.H. Wen, M.H. Shao, Y. Hou, Boron and nitrogen co-doped porous carbon nanofibers as metal-free

electrocatalysts for highly efficient ammonia electrosynthesis, J. Mater. Chem. A 7 (2019) 26272–26278.
[39] X.M. Yu, P. Han, Z.X. Wei, L.S. Huang, Z.X. Gu, S.J. Peng, J.M. Ma, G.F. Zheng, Boron-doped graphene for electrocatalytic N2 reduction, Joule 2 (2018) 1–13.
[40] F. Zhang, X.Y. Liu, M.H. Yang, X.Q. Cao, X.Y. Huang, Y. Tian, F. Zhang, H.X. Li, Novel S-doped ordered mesoporous carbon nanospheres toward advanced lithium metal anodes, Nano Energy 69 (2020), 104443.
[41] Y.M. Liu, Y. Su, X. Quan, X.F. Fan, S. Chen, H.T. Yu, H.M. Zhao, Y.B. Zhang, J. J. Zhao, Facile ammonia synthesis from electrocatalytic N_2 reduction under ambient conditions on N-doped porous carbon, ACS Catal. 8 (2018) 1186–1191.
[42] Y. Jiao, Y. Zheng, K. Davey, S.Z. Qiao, Activity origin and catalyst design principles for electrocatalytic hydrogen evolution on heteroatom-doped graphene, Nat. Energy 1 (2016) 1–9.
[43] L. Shi, Y. Yin, S.B. Wang, H.Q. Sun, Rational catalyst design for N_2 reduction under ambient conditions: strategies towards enhanced conversion efficiency, ACS Catal. 10 (2020) 6870–6899.
[44] Q.Q. Li, Y.L. Guo, Y. Tian, W.M. Liu, K. Chu, Activating VS_2 basal planes for enhanced NRR electrocatalysis: the synergistic role of S-vacancies and B dopants, J. Mater. Chem. A 8 (2020) 16195–16202.
[45] Y. Zheng, Y. Jiao, M. Jaroniec, S.Z. Qiao, Advancing the electrochemistry of the hydrogen-evolution reaction through combining experiment and theory, Angew. Chem. Int. Ed. 54 (2015) 52–65.
[46] C.W. Liu, Q.Y. Li, C.Z. Wu, J. Zhang, Y.G. Jin, D.R. MacFarlane, C.H. Sun, Single-boron catalysts for nitrogen reduction reaction, J. Am. Chem. Soc. 7 (2019) 2884–2888.
[47] Y. Duan, S.N. Sun, Y.M. Sun, S.B. Xi, X. Chi, Q.H. Zhang, X. Ren, J.X. Wang, S. J. Hoong Ong, Y.H. Du, L. Gu, A. Grimaud, Z.C. Xu, Mastering surface reconstruction of metastable spinel oxides for better water oxidation, Adv. Mater. 31 (2019), 1807898.